

SNAKE-fMRI: A modular fMRI data simulator from the space-time domain to k-space and back

Pierre-Antoine Comby, Alexandre Vignaud and Philippe Ciuciu

April 15, 2024

Abstract

We propose a new, modular, open-source, Python-based 3D+time fMRI data simulation software, *SNAKE-fMRI*, which stands for Simulator from Neurovascular coupling to Acquisition of *K*-space data for Exploration of fMRI acquisition techniques. Unlike existing tools, the goal here is to simulate the complete chain of fMRI data acquisition, from the spatio-temporal design of evoked brain responses to various multi-coil k-space data 3D sampling strategies, with the possibility of extending the forward acquisition model to various noise and artifact sources while remaining memory-efficient. By using this *in silico* setup, we are thus able to provide a realistic and reproducible ground truth for fMRI reconstruction methods in 3D accelerated acquisition settings and explore the influence of critical parameters, such as the acceleration factor and signal-to-noise ratio (SNR), on downstream tasks of image reconstruction and statistical analysis of evoked brain activity. We present three scenarios of increasing complexity to showcase the flexibility, versatility, and fidelity of *SNAKE-fMRI*: From a temporally-fixed full 3D Cartesian to various 3D non-Cartesian sampling patterns, we can compare — with reproducibility guarantees — how experimental paradigms, acquisition strategies and reconstruction methods contribute and interact together, affecting the downstream statistical analysis.

Keywords: *fMRI*; *Brain Imaging*; *Accelerated sampling*; *Compressed Sensing*; *Simulation*; *Open Source*; *Python*.

1 Context and Motivation

Functional Magnetic Resonance Imaging (fMRI) has emerged as a powerful tool in neuroscience, enabling scientists to investigate human brain function non-invasively. By measuring blood oxygenation and flow changes (the so-called BOLD effect [Ogawa et al. \(1990\)](#)) induced either in response to external stimuli or spontaneously at rest, task-based and resting-state fMRI have respectively provided invaluable insights into various cognitive processes, intrinsic functional networks, and brain pathology. However, conducting task-based fMRI experiments is an expensive and time-consuming endeavor, often requiring access to advanced imaging facilities and substantial expertise.

The reproducibility of fMRI experiments has shown to be a critical issue in neuroscience. This repro-

ducibility challenge is twofold. First, on a technical side, where applying the same processing pipeline to the same data should yield the same results. This challenge has been addressed by developing and sharing open-source toolboxes [FSL, SPM] and more recently with community initiatives such as fMRIprep ([Esteban et al., 2019](#)), Nipype ([K. Gorgolewski et al., 2011](#)) and the BIDS format ([K. J. Gorgolewski et al., 2016](#)).

Secondly, a more fundamental reproducibility challenge is the ability to replicate the results of an experiment, and this is particularly challenging in fMRI due to multiple sources of intra and inter-individual variability (). To address this variability, large open fMRI data sets have been made available such as the HCP ([Elam et al., 2021](#)), UK Biobank ([Bycroft et al., 2018](#)) or ABCD cohorts ([Casey et al., 2018](#)). With their large population size, they are

able to leverage group-level averaging effect, and also provide invaluable metadata along the functional information. The protocols and processing used in these projects are robust and well tested, but also conservative in their experimental setup (limited spatio-temporal resolution or field-of-view).

However, these data sets do not answer two rising needs for the community: First, the need for higher temporal and spatial resolution() to disentangle fast from slow hemodynamic responses, or to perform laminar fMRI imaging at ultra-high magnetic field. Second, scientific interest in moving to deep phenotyping of a few individuals, as the community is moving toward more personalized medicine and precision neuroscience(Viessmann & Polimeni, 2021). To reach higher resolution, more complex methods on both the acquisition and reconstruction sides are developed. Yet providing a fair comparison between those methods is challenging, due to the reproducibility mentioned above, and the lack of existing ground truth data.

With the rise of computing power, the development of (f)MRI simulators has gained increasing interest in recent years (), with a detailed review in [Welvaert and Rosseel \(2014\)](#). These simulators are designed to provide a ground truth for the fMRI processing pipeline. However, the majority of current simulators are limited to producing (magnitude-only) images, and do not provide raw k-space data. Their use can therefore only be seen as a downstream validation of fMRI preprocessing and statistical analysis tools. Furthermore, the critical step of image reconstruction is not taken into account.

K-space data simulators are also available, but they restrict themselves to anatomical imaging, and are not designed to produce fMRI data. Using complex MR Physics models (), or some approximations (), They are computationally expensive, and their use requires a substantial computational cost and input parameters(pulse sequences parameters, gradients profiles, quantitative maps of tissue properties, etc.) for generating the k-space data associated with a single anatomical volume. Moreover, their main objective is to help the development of new MR sequences, and their use and adaptation for fMRI data synthesis would be achieved at a prohibitive computing cost.

In the search for an absolute ground truth, other solutions than simulation have been proposed, such as active phantoms () or fMRI monitoring with other devices, either to reduce the physiological noise and “clean the BOLD” effect ([Caballero-Gaudes & Reynolds, 2017](#)), or to enhance the reconstruction by removing the acquisition artifacts (). More recently, the development of generative Artificial Intelligence (AI) has opened new opportunity for realistic (f)MRI data synthesis ([Pinaya et al., 2023](#)). However, its expensive computation does not scale for generating high-resolution 3D+t fMRI data, and its lack of control and explainability over the yielded sequence of fMRI volumes discards it for validating downstream tasks such as image reconstruction algorithms.

Overall none of the proposed solutions has succeeded in providing (i) a full control on both the temporally resolved input hemodynamic signal and the output BOLD fMRI time series, (ii) an easy-to-use and reproducible framework through open source software and (iii) a low computational or operational cost.

This paper aims to fill this gap. More precisely, our contribution can be summarized as follows:

We propose an fMRI simulator, named *SNAKE-fMRI* based on the Fourier model of MRI data acquisition, that is able to create all the required k-space data for evaluating the fMRI processing tool-chain: Starting from the definition of an experimental paradigm and the localization of brain activation in a numerical template of the brain, up to the generation of 3D+time k-space data with high temporal resolution (e.g. 100ms). This bottom-up approach, built upon well-grounded realistic anatomical phantom data, allows the fMRI methodologists to use a level playing field and objectively explore and compare various properties of acquisition and reconstruction strategies such as the choice of the sampling pattern (Cartesian vs non-Cartesian readouts), the acceleration factor, etc.

In order to compare the reconstruction methods in more challenging settings, the ground truth data can be degraded in various ways before and during the acquisition process (motion, static field inhomogeneities, thermal and physiological noise, etc.).

The simulator primarily yields a sequence of k-space volumes sampled at a realistic volumetric TR. Additionally, for the sake of completeness, we offer the possibility to yield a sequence of fMRI volumes in the image space by plugging in simple but efficient *volume-wise* reconstruction algorithms.

In the rest of this paper, we first propose a review of available fMRI simulation tools, outlining their strengths and weaknesses (Section 2). Then, we present the design and use of *SNAKE-fMRI* (Section 3 and Section 4 respectively), and finally we showcase three typical simulation scenarios (Section 5), with basic image reconstruction and statistical analysis (Section 6), to illustrate the various possibilities of *SNAKE-fMRI*.

2 Existing software and limitations

The complexity of fMRI data poses challenges in creating a common data generating process. A comprehensive review of publications based on fMRI simulation, as noted in [Welvaert and Rosseel \(2014\)](#), revealed that the absence of a standardized fMRI data synthesis approach hampers reproducibility in fMRI research. This emphasizes the need for improved experimental design reporting and a deeper understanding of fMRI data acquisition processes. Additionally, there exists anatomical MRI simulators focusing on MR Physics, to generate contrast-weighted MR images, but they usually remain confined only to anatomical imaging and thus disconnected from potential use in fMRI.

We provide a broad overview of available fMRI and MRI simulators in Table 1 and focus hereafter on the main alternative to *SNAKE-fMRI*, in increasing order of similarity.

Among existing fMRI data simulation tools, several offer distinct advantages and limitations. The *Virtual Brain* () is an open-source multimodal brain simulator, focusing on the simulation of brain activity using the connectome and subnetwork interaction. It is capable of yielding voxelwise BOLD fMRI time series. However, remains quite complex to master, and is not a dedicated tool for fMRI.

fMRIsim proposed by [Ellis et al. \(2020\)](#), is a Python

package that enables standardized and realistic fMRI time series simulation in the image domain. It allows for the evaluation of complex experimental designs and optimization of the statistical power. However, it mainly focuses on single-subject simulations and requires manual parameter setting or estimation from real data. It was inspired by a parent R package *neuroRsim* ([Welvaert et al., 2011](#)). Nevertheless, it primarily deals with magnitude data and uses additive noise settings, which might restrict its applicability to specific simulations or use cases (e.g. limited resolution).












SimTB, introduced by [Erhardt et al. \(2012\)](#), is a MATLAB toolbox specialized in simulating fMRI time series using a separable spatio-temporal model. It offers extensive customization options, including spatial sources, experimental paradigms, tissue-specific properties, noise, and head movement. *SimTB* is equipped with both a graphical user interface and scripting capabilities. Again, no k-space data is available.




The *POSSUM* simulator, as outlined by [Drobnjak et al. \(2006\)](#), offers a comprehensive approach to the impact of various artifacts encountered in fMRI data acquisition. *POSSUM* accurately simulates these artifacts using Bloch equations and a geometric definition of the brain. However, its computational cost is heavy, making simulations of full brain at high resolution prohibitive. Additionally, it currently only offers the possibility to yield Cartesian data in k-space. The fMRI analysis is deferred to the *FSL* library, and no comparison with the ground truth is provided as an outcome of the toolbox.

3 From ground truth to acquisition: The main characteristics of *SNAKE-fMRI*

SNAKE-fMRI has been designed as a modular, fully reproducible fMRI simulator capable of generating k-space data efficiently. This makes *SNAKE-fMRI*, a tailored solution for benchmarking the fMRI processing pipeline end-to-end or for focusing on specific aspects such as the production of k-space data or image-domain time series. In what follows, we give a broad overview of the main advantage of *SNAKE-fMRI*. They will be then illustrated in Section 5 and Section 6

Table 1: Summary of characteristics of different fMRI data simulators.

	Simulator Name	Licence	API	Sim. Domain	Required External Data	Interface	Reconstr.	Ecosystem
	TVB (Sanz Leon et al., 2013)	GPL-3.0		Image		GUI/script	N/A	N/A
	Jemris (Stöcker et al., 2010)	GPL-2.0		Bloch		GUI	ISMRMD raw data	N/A
MRI Simulator	ODIN (Jochimsen et al., 2006)	GPL-2.0		Bloch	Tissue Maps, Sequence	c++/GUI	FFT	OdinReco
	MRILab (Liu et al., 2017)	BSD-2		Bloch	Preset Macros	GUI	FFT Non-Cartesian	GUI Gadgetron
	Bloch-Solver (Kose & Kose, 2017)	Proprietary		Bloch	Tissue Maps,	script	FFT	N/A
	POSSUM (Drobnjak et al., 2006)	FSL		Bloch	Tissue Maps Sequence, Events	CLI	FFT	FSL
fMRI Simulator	Neurolib (Cakan et al., 2023)	MIT		Image	Connectivity Matrices	script	N/A	Jupyter
	SimTB (Erhardt et al., 2012)	Open Source		Image	Spatial Maps, Events	GUI	N/A	MATLAB
	NeuroRSim (Welvaert et al., 2011)	GPL-2.0		Image		script	N/A	N/A
	fmriSim (Ellis et al., 2020)	Apache-2.0		Image		script	N/A	Brainiak
	SNAKE-fMRI	MIT		Kspace Image	Configuration files	script/CLI	Any (4D methods)	Any

API Languages:  Python  MATLAB®  C++

3.1 Modular Approach

SNAKE-fMRI adopts a modular approach for the simulation of fMRI data, leveraging object-oriented programming as illustrated in Figure 1. A core simulation object will be modified and enriched by so-called *handlers*, each of them being responsible for a specific part of the model. Section 4 describes in detail the core handlers available in SNAKE-fMRI, it is also possible to create and use custom ones as detailed in Section A.1 of the supplementary material.

Typically, the simulation begins with the definition of an anatomical phantom of the brain in the image domain, and proceeds to add BOLD contrast and various noise sources before generating the k-space data. As shown in Figure 1 those handlers can be chained to produce complex behaviors from

simple operations.

After simulating the data of interest (for instance a series of k-space volumes and the associated sampling pattern), the simulation can be completed with image reconstruction of the fMRI sequences and statistical analysis.

At the end of the processing and analysis chain, it is possible to compare the reconstructed data with the ground-truth simulation, and evaluate the effect of acquisition parameters (SNR, acceleration factor, etc.) on the image quality as well as on the fMRI statistical analysis.

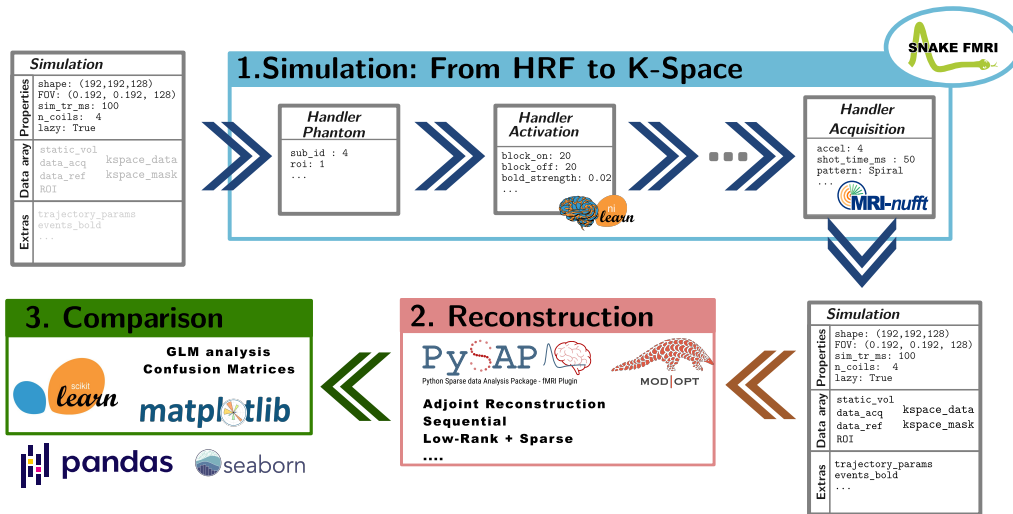


Figure 1: Modular design of the simulator, and ecosystem of packages used in *SNAKE-fMRI*. 1. Each handler manages a particular aspect of the fMRI data acquisition. A *SimulationData* object containing all the data and metadata of the simulation is fed into a chain of handlers, each adding or modifying fields of the simulation. 2. Then the completed simulation (notably with k-space data) can be used as input for reconstruction methods, producing an estimation of the fMRI time-series. 3. Finally the reconstructed data is compared to the ground truth used in the simulation using standard statistical tools, such as first-level GLM regression analysis, and the quality of the detection of activating voxel post-reconstruction and regression analysis can be assessed by comparing with a ground-truth region of interest, using standard confusion matrix metrics (e.g. precision, recall, sensitivity).

3.2 K-Space data generation

One of the critical aspects of *SNAKE-fMRI* is the generation of k-space data. Yet the discrete approach of k-space data acquisition, providing a finite volume at a specific time resolution, is incompatible with the continuous and analogous behavior of neuronal activity. We thus dissociate the temporal resolution when simulating brain activity (typically set to 100ms) from the temporal resolution during the MRI data acquisition in k-space (with a TR_{vol} of 2500ms). In order to do so, we proceed as follows:

During a real scan, as the acquisition of k-space data proceeds, brain activity is also evolving, and spin relaxation also takes place. Modeling all these aspects would be computationally prohibitive, and thus we propose a simplified approach where the signal is considered constant during the acquisition of a single shot, thereby neglecting the relaxation aspect of MR physics, as depicted in Figure 3. This tenable assumption is also made at the reconstruction step, allowing us to use the Fourier transform as the forward model of fMRI acquisition and maintain low numerical complexity for simulating all k-space data for the whole fMRI sequence. The *handler* responsible for the acquisition is further described in Section 4.3

3.3 Performance, Reproducibility and Scalability made easy for scientist in neuroimaging

3.3.1 Performance

Storing the full high spatio-temporal simulation would be quite demanding (100Go of RAM for a single $192 \times 192 \times 128$ volume at 100ms to simulate 5 minute of an 1mm isotropic fMRI paradigm) and each substantial change, like adding noise would create a new copy of this data. Instead, we propose to yield the data lazily, as each time point in the series can, most of the time, be computed from a sequence of transformations applied to a single anatomical volume (for instance, adding the BOLD contrast, noise, or using motion parameters). Such base phantoms are available in *SNAKE-fMRI*, as depicted in Figure 2. In practice, this lazy mechanism allows for the simulation of a single frame or a subset of frames easily. This results in little computational overhead and enables embarrassingly

parallel approaches to acquire those volumes. All numerical experiments were conducted on the following hardware: 20-Cores Intel Xeon Silver CPU and an NVIDIA RTX 5000 GPU.

3.3.2 Reproducibility

Enabling reproducibility in the study of fMRI processing methods is at the heart of *SNAKE-fMRI* development. This simulator can be installed directly from the Python package archive and its core only depends on standard and well-tested Python packages. Simulation setup can be shared through `.yaml` files describing the recipe for building a simulation, as shown in Section A.2 of the supplementary material.

3.3.3 Scalability

Furthermore, based on the `hydra` framework we are able to run multiple simulations with different parameters or handlers and to perform image reconstruction of fMRI volumes and simple statistical data analysis to compare competing approaches. It also allows us to scale up simulations from a single laptop to high performance computing clusters.

4 Description of available handlers

SNAKE-fMRI comes with a collection of basic *handlers* for creating simple simulations. Defining a handler is also made easy, as detailed in Section A.1 of the supplementary material.

4.1 Phantom and brain activation

To produce a sequence of fMRI volumes we start with the specification of an anatomical phantom, such as BrainWeb (Aubert-Broche et al., 2006). Using the provided fuzzy segmentations of tissue classes, we produce a realistic T2* contrast with standard quantitative tissues-specific values for a given field strength, and create a region-of-interest (ROI) from a subset of the gray-matter tissue mask. A 2D phantom (Guerquin-Kern et al., 2012), as well as the Shepp-Logan phantom (Gach et al., 2008), with their ROI, are also available. Those phantoms

are available in the `snkf.handlers.phantoms` module.

The fMRI time series is then synthesized by adding a BOLD response, which consists in convolving an experimental design with a hemodynamic response function (HRF) (). The current experimental paradigms (such as block and event-related designs) are available in the `snkf.handlers.activation` module.

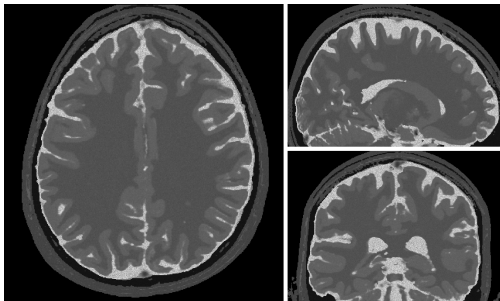


Figure 2: Generated T2*-weighted Brainweb phantom at 0.5mm isotropic spatial resolution.

4.2 Adding noise sources

Creating an fMRI time series by adding evoked brain activity in specific ROI is too idealistic, thus we can superimpose layers of noise to the simulation to obtain more realistic data. A simple example is, for instance, the addition of spatial Gaussian white noise to prescribe a specific SNR. This noise can be included either in the image domain prior to the acquisition or in the k-space during the acquisition. This closely follows the assumptions made on the model at the reconstruction step where the goal is often to solve an inverse problem with additive Gaussian noise (Fessler, 2019).

In the fMRI methods literature, the spatial SNR is computed on the reconstructed anatomical image, and the study of experimental and MR sequence parameters (field strength, coil array, flip angle, TR and TE, etc.) impact on the SNR is a continuous topic of research (). Similarly, the temporal SNR or tSNR, computed voxelwise, provides some insights on the quality of time series, but has shown limitations (Jamil et al., 2021).

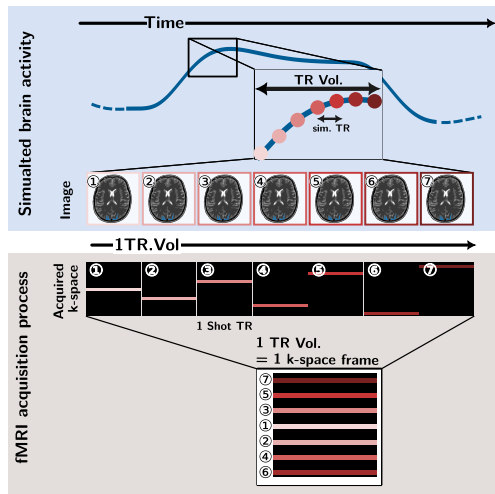


Figure 3: Acquisition Method implemented in SNAKE-fMRI: The case represented is simplified to a 2D Cartesian case (e.g. a projected view of a 3D non-accelerated EPI scheme). Each shot (or plane in 3D EPI) of the k-space sampling pattern is acquired separately from an on-the-fly simulated volume.

In SNAKE-fMRI, as described hereafter, we adopt the following definitions for the SNR, depending on the data available at a particular stage of the simulation. μ and σ represent the average and standard deviation operators, respectively

- *Phantom SNR*: represents the intrinsic SNR level of the phantom. It is computed as:

$$SNR_p = \mu(x \in B) / \sigma(x \in V) \quad (1)$$

Where B and V represent two distinct regions of the 3D brain phantom x under consideration. For instance, in Figure 2 V would be some corner region of volume x , and B all voxels where we can get some signal in the brain.

- *Input SNR*: represents the prescribed SNR in the image. It is used to compute the spatial noise variance σ_n^2 that is added to the simulation.

$$SNR_i = \mu(x \in B) / \sigma_n. \quad (2)$$

- *Experimental SNR*: computed after image reconstruction separately for each fMRI volume $x \in$

$\mathbb{C}^{T \times N_x \times N_y \times N_z}$ acquired at time t_k

$$SNR_{\text{exp}}(t_k) = \mu(x(t_k, :) \in B) / \sigma(x(t_k, :) \in V). \quad (3)$$

- *Experimental tSNR*: computed after image reconstruction separately for each voxel u_i

$$tSNR_{\text{exp}}(u_i) = \mu(x(:, u_i)) / \sigma(x(:, u_i)). \quad (4)$$

A study on the interaction of these metrics in *SNAKE-fMRI* is provided in Section B of the supplementary material.

More structured noise sources (e.g. motion and physiological noise) can be envisaged and the wide variety of parameters choice and methods for those noise sources is beyond the scope of this article. Future work (open to contributions) will go into more detail on the implementation of those noise sources. The noise handlers are available in the `snkf.handlers.noise` module.

4.3 Acquisition

The acquisition process in *SNAKE-fMRI* is modeled using a Fourier transform, and represented in Figure 3. Using MRI-NUFFT (Comby et al., 2024) it is also possible to acquire non-Cartesian sampling patterns in k-space.

The characteristic global observation time for a shot in a $T2^*$ weighted MR sequence used for fMRI is in the order of 25 to 50 ms, which is shorter than the period of significant physiological signals such as breathing and heartbeat (roughly 1s) or the support of the canonical hemodynamic response function (20 to 30s). Thus, simulating and acquiring a complete volume for each shot is already a faithful approximation of the acquisition process in fMRI. In practice, the temporal resolution at simulation can also be relaxed to group multiple shot (for instance, a simulation time of 100 ms for four shots of 25 ms), that are then acquired simultaneously, reducing the memory and computational cost of the simulation.

In practice each volume is the result of data acquisition along segmented k-space trajectories in 3D. The data supported by each shot in k-space is collected using the Fourier Transform model. Then

multiple shots are gathered to form a volume in k-space and define a specific frame in the fMRI sequence.

If requested, the simulation module also provides a multi-coil acquisition setup, where sensitivity maps are generated and used for the acquisition. Those sensitivities maps can also be made available for the reconstruction, or left aside for a calibration-less reconstruction (`calibless`). Moreover, this model can be further extended to take static and dynamic B_0 -inhomogeneities into account. The dynamic fluctuations of B_0 can actually be modeled at the same temporal resolution of the simulation (Sutton et al., 2003)

The acquisition handlers are available in the `snkf.handlers.acquisition` module.

4.4 Standardized data exchange

Extensibility is at the heart of *SNAKE-fMRI*. In particular, we provide handlers to import standard data format (`.nii`, `.npy`, `.csv`, ...) for any parameter of the simulation. Similarly, the data can be exported to these formats, as well as to the ISMRMRD raw k-space format (Inati et al., 2017), to enable data exchange with other reconstruction toolboxes (such as SigPy, Ong Frank and Lustig Michael (2019) or BART, Uecker et al. (2015))

Handlers to save and or load parts of the simulation data are available in the `snkf.handlers.io` module.

5 Numerical experiments

In this section, taking advantage of *SNAKE-fMRI* modularity and scalability, we demonstrate the use of a controlled simulation framework to explore the potential benefits and challenges of moving to higher resolution in space and time for fMRI experiments. Results and analysis are presented in the next section.

First, we detail three simulated scenarios of increasing complexity (from 3D Cartesian low spatial resolution to 3D non-Cartesian high temporal or spatial resolution) with basic reconstruction and sta-

tistical analysis pipeline. All scenarios simulate a five-minute long full-brain run of a simple visual stimulation using a standard block-design paradigm, which alternates 20s-on and 20s-off periods. In response to visual stimuli, we induced a 2% of contrast change as the elicited BOLD signal in a region of interest, which is defined from a fuzzy segmentation of the gray matter intersecting an ellipse located in the occipital cortex. White Gaussian noise was added to all scenarios with $SNR_i = 10$ in the image space, before performing the acquisition. For a detailed explanation on the SNR setting, see Section 4.2.

The three scenarios as well as their computational cost are summarized in Table 2. All simulation were

Table 2: Brief descriptions of simulated scenarios and their computations requirements. N_c, N_s and n_{jobs} specify respectively the number of coils simulated, the number of shots acquired to create a k-space volume and the number of frames simulated concurrently. SoS is a shorthand for Stack-of-Spirals trajectory, SPKL for 3D-SPARKLING trajectory (Chaithya et al., 2022). Hardware Configuration is described in Section 3.3.1.

Setup	Res.	TR_v	N_c	N_s	Traj.	n_{jobs}	Time	RAM	VRAM
							(s)	(GB)	(GB)
S1	3mm ³	2.2s	1	44	EPI	1	11	18.21	0
S2	3mm ³	0.7s	8	14	SoS	2	41	39.31	0.42
S3	1mm ³	2.4s	32	48	SPKL	4	2535	45.43	4.73

run on a 20-Cores Intel Xeon Silver and an NVIDIA RTX 5000 GPU.

5.1 Scenario S1: 3D Cartesian fully sampled

As a first validation example we simulated the acquisition of 3D Echo Planar Imaging (EPI) data, as an implementation of a 3D Cartesian readout. Each slice was fully sampled at a 3mm isotropic resolution (matrix size: $64 \times 60 \times 44$), the parameter file describing this scenario is detailed in Section A.2 of supplementary material. With a $TR_{shot} = 50ms$ for acquiring a full EPI plane, we have a volumic temporal resolution $TR_{vol} = 2.2s$. Since the data is collected at the Nyquist rate, we restrict ourselves

to a single coil acquisition. This simple configuration can be simulated on a standard laptop in less than a minute, a similar configuration acquired with POSSUM would have taken several hours, for fewer slices (see Drobnjak et al. (2006), Table 2), due to its more mathematically involved model related to MR physics.

5.2 Scenario S2: 3D stack of Spiral VDS

The second scenario explores the possibility of SNAKE-fMRI for accelerated imaging based on Compressed Sensing (CS) for data acquisition and image reconstruction. The resolution and FOV remains the same as for Scenario S1, but we aim for faster temporal resolution. To do so, we perform first an acceleration over the 2D plane ($k_x k_y$) using an in-out spiral acquisition (with $TR_{shot} = 25ms$, twice as fast as a full EPI plane), and second a variable density sampling along k_z that evolves across scans (10% of center planes continuously acquired, AF=4 on the periphery), as depicted on Figure 7a. This results in 14 spiral shot acquired per volume, overall reaching $TR_{vol} = 0.7s$ volumic temporal resolution. To maintain a good SNR, we simulated a multi-coil acquisition with $N_c = 8$ receivers.

The k-space readout is illustrated in Figure 7a. Using GPU-accelerated NUFFT the simulation of the acquisition at 3mm isotropic resolution takes around a minute of computation (Table 2). CPU based NUFFT implementation is also available but remains slower.

This approach has already been studied numerically and experimentally in Petrov et al. (2017) with image reconstruction strategies that take advantage of this acceleration mechanism, such as low-rank + sparse regularization (). Here we are limiting the reconstructions strategies to frame-wise approaches, described in Section 5.4.

5.3 Scenario S3

Last, we illustrate the use of a full 3D non-Cartesian sampling pattern, by simulating a 3D SPARKLING acquisition () over $N_c = 32$ coils at a 1mm-isotropic resolution and a volumic TR of 2.4s. 3D

SPARKLING implements a variable density sampling according to a prescribed sampling density in k-space, while complying with the hardware constraints on gradient magnitude G_{\max} and slew rate S_{\max} . It allows us to further accelerate the acquisition process compared to Scenario 2 in order to reach higher spatial resolution.

The parameters for this scenario are based on the experimental setup of [empty citation](#), which is described in Section 5.4, and on Figure 4, top row. Here only a simulation with a static sampling pattern across frames is generated. The study of a dynamic 4D accelerated sampling pattern for fMRI and its optimal reconstruction strategy remains an active area of research and is currently beyond the scope of this simulator.

5.4 Scenario 2 & 3: Reconstruction strategies

For simplicity, as the primary focus here is on the simulation of k-space data, we will restrict ourselves to a classical, frame-wise CS based image reconstruction with standard sparsity enforcing regularization term in the wavelet domain:

$$\hat{\mathbf{x}}_t = \arg \min_{\mathbf{x} \in \mathbb{C}^N} \frac{1}{2} \sum_{\ell=1}^{N_c} \|\mathcal{F}_t \mathcal{S}_\ell \mathbf{x} - \mathbf{y}_{t,\ell}\|_2^2 + \mu g(\Psi \mathbf{x}). \quad (5)$$

This means that each frame t is reconstructed independently of the other as we use the following notation:

- \mathcal{F}_t is the Fourier transform operator for the trajectory at time t .
- \mathcal{S}_ℓ are the sensitivity maps
- Ψ is a spatial sparsity promoting transform, here an orthogonal wavelet transform such as `sym-8`.
- $\mu g(\cdot)$ is the regularization function, here a classic ℓ_1 -norm is used.

The cost function to be minimized is convex but non-smooth. Its global minimizer can be found iteratively using a wide range of proximal gradient methods

with possible acceleration schemes such as FISTA, POGM (). As illustrated in Figure 1, CS based image reconstruction was performed using the PySAP library (Farrens et al., 2020), and the implementation of the POGM algorithm (Kim & Fessler, 2018). To reduce the number of free parameters, the regularization parameter μ was estimated using Stein’s Unbiased Risk Estimate (SURE) (Donoho & Johnstone, 1994), and then set to $\mu = 1.2$ for all reconstructions strategies.

The versatility of SNAKE-fMRI allows us to propose a restricted benchmark on two acquisition strategies, a *static* vs *dynamic* scenario. In the former, the same k-space trajectories are used for all frames whereas in the latter a new randomly picked k-z coordinate was used for each and every frame as shown in Figure 7a. Then iterative CS reconstruction of each frame described in Figure 4 was carried out either:

- naively by computing an *adjoint* NUFFT reconstruction.
- independently to solve (5), in a *cold-start* fashion, see Figure 4, top row.
- strategically using a *warm-start* strategy based on the output image of frame n to reconstruct frame $n + 1$, see Figure 4, middle row.
- smartly using an extra *refined* initialization where the last reconstructed volume using warm-start was used as new setup for all other frames. See Figure 4, bottom row.

All these variations are based on the frame-based reconstruction of k-space data, and as such provides a memory-efficient implementation, yet they don’t leverage the whole 4D fMRI k-space data at once, in contrast to low-rank+sparse methods()

6 Results for the different scenarios

6.1 Scenario S1

In Scenario S1 the data is fully acquired and reconstructed directly using the inverse FFT. The

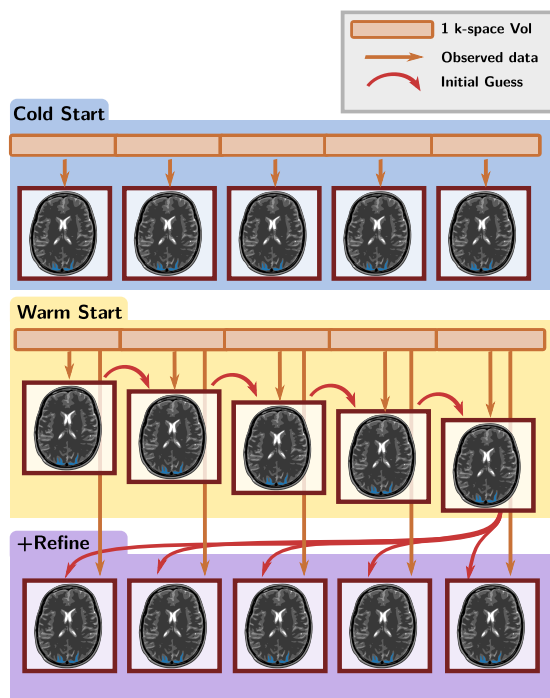


Figure 4: Different methodologies for sequential reconstruction used in Scenario S2.

low spatial and temporal resolution translates itself in a good experimental SNR ($\text{med}(SNR_{\text{exp}}) = 38.09$, $\text{med}(tSNR_{\text{exp}}) = 25.64$), and the statistical analysis (Figure 6, $AUC = 0.926$ for Precision/Recall) shows very good performances for detecting evoked brain activity in the occipital ROI: Clear BOLD signal variations are visible in the ROI (Figure 5) This validates the forward model chosen for SNAKE-fMRI. Getting access to the ground-truth ROI allows us to validate that GLM analysis performed well. Impact of the SNR_i on the reconstruction is presented in Section B of the supplementary material.

6.2 Scenario S2

Scenario S2 focuses on the joint effect of optimizing acquisition and reconstruction strategies for acceleration purposes, and is the main example to demonstrate the versatility of SNAKE-fMRI. As described in Section 5.2 we have 2 different acquisition strategies (static vs dynamic stack of spirals) and 2 varia-

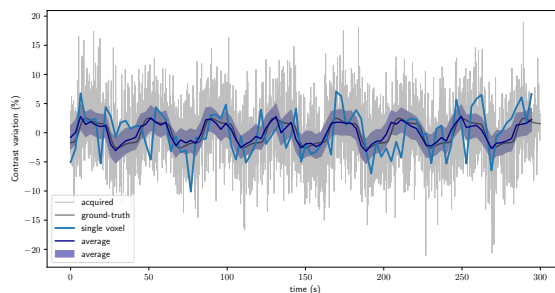


Figure 5: Scenario S1: Time series of a voxel inside the ROI, eliciting evoked brain activity. A noisy signal ($SNR_i = 10$, light gray) is acquired shot-wise and reconstructed volume-wise (blue). Average over the ROI is also depicted in purple.

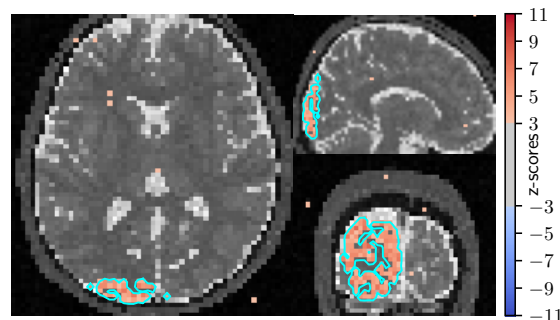
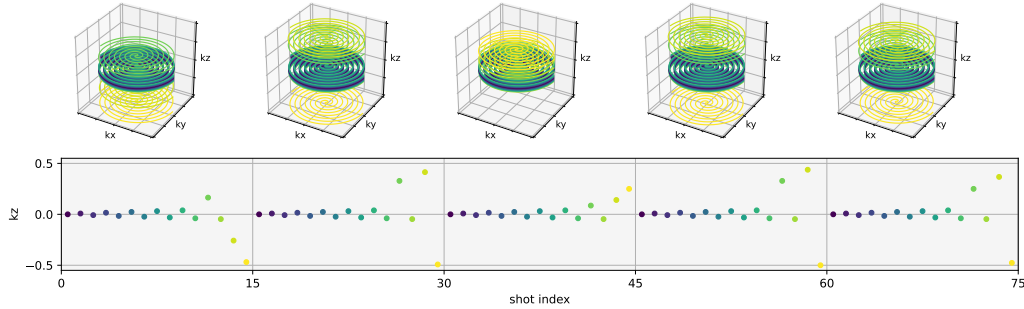


Figure 6: Scenario S1: Activating voxel detected ($p < 0.001$) for Scenario S1. The k-space is fully sampled and the analysis pipeline can retrieve the activated regions, matching the original ROI, outlined in cyan. A few false positives are also found, due to a non-ideal SNR.

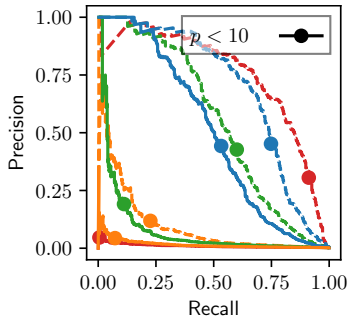
tions of reconstruction methods (cold vs warm initialization for each volume). The dynamic acquisition has also been reconstructed in a two-step process, namely combining a warm start strategy with a fine-tuning of each frame afterwards. The 4D spatio-temporal data being known, we are able to assess each configuration with respect to image quality as well as to statistical performances for detecting brain activity with a good sensitivity/specificity or precision/recall trade-off.

Based on these six configurations and the results shown in Figure 7 we are able to make the following claims.

(a) Example of dynamic trajectories Stack of spirals acquisition strategy used in Scenario S2. AF=32 for visualization purposes. Central slices of k-space are always acquired, higher frequencies are sampled at random.

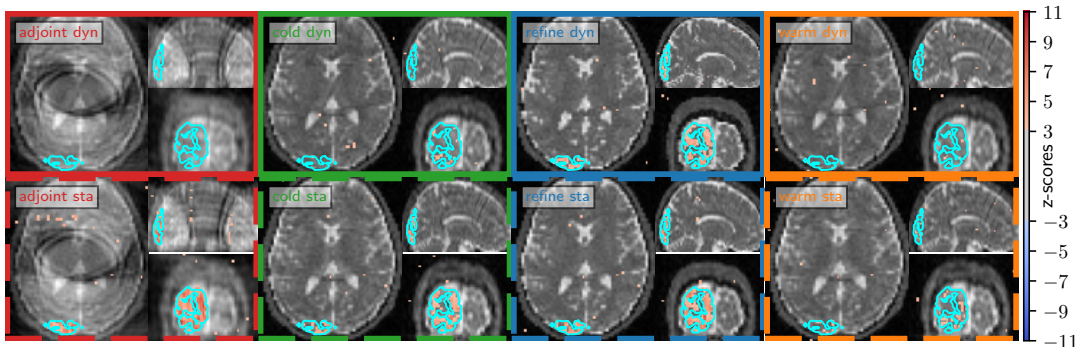


(b) Precision-Recall Curve for reconstruction methods.



(c) Summary of image quality, statistical metrics and Reconstruction time Hardware configuration is described in Section 3.3.1.

Setup	SSIM		PSNR		AUC	BACC	Time
	First	Last	First	Last			
adjoint sta	0.45	0.45	16.87	16.95	0.75	0.91	25"
cold sta	0.74	0.74	23.59	23.34	0.55	0.60	41'04"
refine sta	<u>0.80</u>	0.81	<u>25.831</u>	25.89	<u>0.67</u>	<u>0.75</u>	67'21"
warm sta	0.74	0.80	23.59	25.92	0.09	0.22	37'55"
adjoint dyn	0.48	0.46	16.73	16.97	0.01	0.00	2'21"
cold dyn	0.78	0.75	24.12	23.15	0.08	0.11	37'29"
refine dyn	0.84	0.83	28.98	28.83	0.50	0.53	70'21"
warm dyn	0.75	0.83	24.12	28.83	0.01	0.07	49'23"



(d) Z-score activation detection map ($p < 0.001$) and comparison with ground-truth ROI (outlined in cyan) The background is the first reconstructed fMRI volume in the sequence.

Figure 7: Results for the Scenario S2 (res=3mm, $TR_{vol}=0.7s$) using *static* vs *dynamic* acquisition strategies and various initializations for image reconstruction. Static, i.e. temporally fixed, acquisition with basic reconstruction provides the best statistical scores, but degraded image quality metrics. More complex acquisition-reconstruction combinations (such as dynamic acquisition with refined reconstruction) provides the best image quality over the fMRI run, while retaining good statistical performances.

6.2.1 The warm start initialization is key in dynamic acquisition for improved performances

Image quality is improved both for static and dynamic acquisitions when a warm start strategy is applied (see Figure 7c). Indeed, as information is shared forward between frames, we observe a gain in both SSIM and PSNR scores between the first and last frame. This is especially effective for dynamic acquisition, as each frame brings new information from under-sampled frequencies. In that context, the warm start strategy exploits this information to improve the reconstruction of the upcoming frame. To maintain a consistent image quality over the whole fMRI run (i.e. sequence of fMRI volumes), the refined approach is necessary. This means that the last reconstructed volume based on the warm-start approach becomes the new initialization for all other frames.

Moreover, the absence of shared information across frames when using dynamic under-sampling patterns introduces temporal incoherence and add subsampling pattern artifacts and is thus detrimental to image quality and statistical performances unless appropriate reconstruction methods (e.g. k-t sparse techniques such as FOCUSS (Ye et al., 2007)), which specifically exploit temporal incoherence, are used. However, the latter were not tested in this paper and are left for future comparison with the refined initialization technique.

6.2.2 Static strategy boosts sensitivity at the cost of specificity and image quality

The static acquisition strategy provides the best statistical performances, as it is able to detect the activation with the highest precision and recall scores, even for the naive zero-filled reconstruction method (see 7c and 7d). However, the image quality is severely degraded in those cases. These performances must be put in perspective with the particular noise configuration that was simulated here. Using a static acquisition strategy, any spatial aliasing artifact is repeated over the whole time series, and potentially reinforces activation detection, even in the presence of false positives, which are typically seen in the reconstruction based on the adjoint

NUFFT operator. This statement is no longer true for a dynamic acquisition, as the aliasing pattern varies across frames, hence the false positive rate remains low.

6.2.3 Image quality is not a proxy for good statistical performances

Comparing the metrics in Figure 7c, we can see that the best image quality is not always associated with the best statistical performances. A striking example is the adjoint NUFFT reconstruction, which provides the worst image quality with strong aliasing artifacts (see Figure 7d), yet provides the best statistical performances. Additionally, Consistency of image quality (even if degraded) over the whole fMRI run also matters, as warm-start reconstruction (where the image quality improve over time) shows very poor statistical performances.

Getting the best of both worlds is possible using the refined strategy, as it provides the best image quality over the whole sequence of fMRI volumes, while retaining good statistical performances. The benefit of using a static or dynamic acquisition in this setup is less clear. Yet, dynamic acquisition strategies have shown some great potential for increasing the temporal resolution, while maintaining good image quality. It is also expected that more complex noise sources (such as motion or physiological artifacts) would help discriminate these two strategies.

6.3 Scenario S3

Last, we present results generated from Scenario S3 (res=1mm iso, $TR_{vol}=2.4s$) as a proof of concept of the scalability of SNAKE-fMRI to high spatial resolution fMRI.

Here we compare the adjoint NUFFT operator with the sequential (cold-start) CS reconstruction, following the setup of the previous experimental work described in <empty citation>. We retrieved similar activation maps, comforting the choice of $SNR_i = 10$ for the noise in the simulation to make it as much realistic as we can.

In this high spatial resolution regime, we see the benefit of using an optimized under-sampling pat-

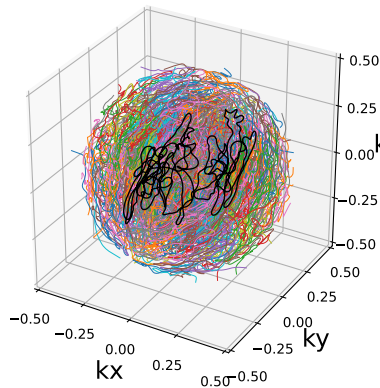


Figure 8: 3D SPARKLING trajectory used in S3: 48 shots, with $TR_{shot}=50ms$.

tern with respect to a target sampling density. No aliasing artifacts are visible on the zero filled reconstruction with density compensation (Pipe & Menon, 1999). With GPU Acceleration, the Sequential Reconstruction took 16'10" to complete. Using a CS based approach both image quality and statistical performances are improved as shown in Figure 9 This scenario opens the door to more complex acquisition and reconstruction strategies to reach higher spatial and temporal resolution. Such case studies are now made possible with SNAKE-fMRI.

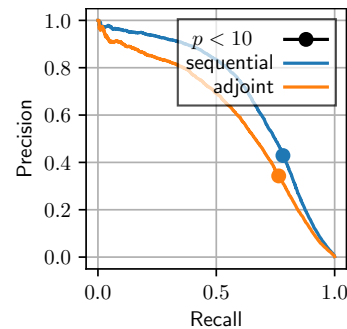
7 Discussion

We provide a new open-source simulation software, SNAKE-fMRI with an easily extensible core for modeling all aspects of the fMRI problem.

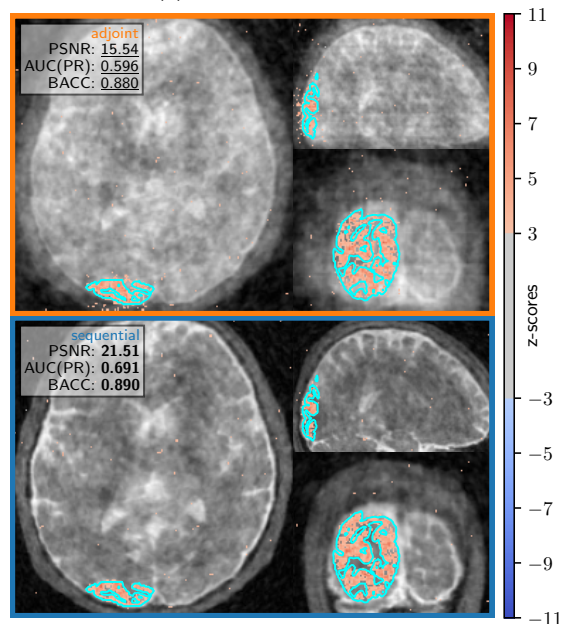
7.1 Comparison between scenarios

The three scenarios showcased in Section 5 and 6 provide complementary views for the comparison of acquisition and reconstruction strategies.

Scenario S1 provides a low spatial and temporal resolution, uses basic reconstruction methods and shows the potential of SNAKE-fMRI to provide a ground truth for detecting evoked brain activity. Beyond providing a simple and fast validation case for the simulator, this scenario could be used for instance to compare the statistical performances



(a) Precision-Recall curve



(b) Activation maps for S3.

Figure 9: Results of scenario S3 ($res=1mm$, $TR_{vol}=2.4s$). Using sequential cold-start CS reconstruction we obtain improved statistical performance compared to a direct density-compensated adjoint NUFFT operator.

of different competing experimental paradigms regarding the number and duration of stimuli at fixed acquisition time.

Scenario S2 explores a low spatial, high temporal resolution setup and provides a large panorama of possible acquisition and reconstruction strategies. It shows the potential of SNAKE-fMRI to provide

a benchmark of competing techniques both during acquisition (static vs dynamic stack of spirals) and image reconstruction, notably in the CS setting. Of course this benchmark could be complemented in the future by adding for instance low-rank + sparse methods or even deep-learning approaches using plug and play algorithms with specifically trained denoiser. Interestingly, from its current implementation, we observed that the best image quality is not always associated with the highest statistical scores, and that the warm start strategy is key in dynamic acquisition for improved statistical performances.

Finally, Scenario S3 provides a high spatial and low temporal resolution setup, reaching the limits of current fMRI acquisition strategies for whole brain coverage. Unlike Scenario S2, the SPARKLING under-sampling pattern does not show aliasing artifacts, even at high spatial resolution. From the comparison with the ground truth we are able to show that using CS Reconstruction we obtain better statistical performance than with a direct density-compensation adjoint. Yet, the practical application of SPARKLING to fMRI has shown some challenges related to dynamic B_0 inhomogeneities (Amor et al., 2023), making its usage difficult in real life.

Overall, these three scenarios should be considered as an upper-bound in terms of image quality and statistical performances for prospective validation as actual data acquisition and image reconstruction face additional issues such as imperfection in coil sensitivity estimation, presence of motion artifacts, off-resonance effects due to static and dynamic B_0 inhomogeneities. Degrading the forward model (without improving the reconstruction algorithms) by taking additional artifact sources into account is expected to yield lower quality results in this setup.

7.2 Extending the simulator

As SNAKE-fMRI is an open source software, external contributors from the fMRI community are invited to participate in its extension to help us refine the forward modeling for handling multiple sources of artifacts that contaminate actual fMRI data. Among possible fMRI signal perturbations,

one may think of modeling the contributions of rigid head motion either in k-space or in the image domain, temporal aliasing artifacts due to physiological rhythms (heart beat or breathing rate) that are not sampled fast enough, static and dynamic B_0 field inhomogeneities that induce blurring, signal loss and geometric distortions on images as well as changes in the k-space trajectories. Adequate fMRI acquisition and/or reconstruction methods could be considered or developed to mitigate these additional sources of perturbation.

Similarly, more complex brain activation patterns spread over multiple ROIs could be designed with variations in the HRF shape for instance, following the seminal work of PyHRF (Vincent et al., 2014), or by using sources based on existing fMRI data, as well as using complex-valued BOLD activation (Z. Chen et al., 2018). Moreover, results from other fMRI simulators, such as the Virtual Brain (Schirner et al., 2022) could be used as input reference data for SNAKE-fMRI.

However, adding layers (and their potential heavy parameterization) to the simulation will also induce a potential loss in explainability for the effect on downstream applications, and will likely need to develop more elaborated metrics to evaluate their relevance to the problem at hand.

7.3 Exploring the effect of tuning acquisition and reconstruction together

The first results obtained with SNAKE-fMRI show the criticality of matching and tuning the experimental design, acquisition, and reconstruction strategies to obtain the best quality in the downstream analysis. In particular, fast event-related designs with short inter stimulus intervals require a higher temporal resolution to be properly detected. Yet, moving to high temporal resolution would induce a drop in effective SNR. This can be overcome by using more complex acquisition and reconstruction methods that leverage temporal redundancy in the k-space data with global a priori such as a low-rank+sparse (), Similarly, the *refine* strategy introduced in Scenario S2 shows some great potential both for static and dynamic acquisition schemes, and will be the subject of future development.

To the best of our knowledge, as summarized in Table 1, SNAKE-fMRI is the only open source fMRI data simulator that can provide arbitrary fMRI k-space data efficiently. It is also the only one that can be used to benchmark reconstruction methods in an automated manner. Comparing it to other simulators is not a straightforward task, as the competitors are not designed for the same purpose. This comparison might actually be biased by different assumptions made in the computation of the forward model, that is the production of k-space data. Yet, the different scenarios presented in this paper define a good starting point for such a comparison. Further, the increasing complexity of these scenarios goes beyond the capabilities of existing simulators.

7.4 More than a simulation tool

The modular approach of SNAKE-fMRI also allows for other uses than simple simulations. First, the combination of the runner scheduling and analysis modules provides a reliable benchmark for image reconstruction methods (even for a single anatomical volume).

Then, each handler can also be viewed (and used) as a data augmentation layer for supervised deep learning methods, giving new opportunities for the fMRI image reconstruction problem as the supervised setting is not applicable in that context due to the lack of ground truth data. Hence, SNAKE-fMRI could be used either to train on synthetic fMRI data deep neural networks dedicated to fMRI image reconstruction. These models might be fine-tuned afterward with transfer learning on real data sets. Alternatively, SNAKE-fMRI might serve as a data augmentation tool.

8 Conclusion

In this paper, we have proposed a new fMRI data simulator, called SNAKE-fMRI that is packaged in an open source Python software with professional standards, thereby offering to both ISMRM and OHBM communities the opportunity to advance the field of optimal fMRI data collection at low scanning cost. More specifically, SNAKE-fMRI is purposely

designed to assess the impact of massively undersampled 3D non-Cartesian readouts aiming to reach unprecedented spatial resolution while maintaining whole brain coverage, good image quality and ability to detect tiny BOLD effect through statistical guarantees.

In vivo experiments show limitations (notably reproducibility issue and cost) on how they can be used to explore new acquisition and reconstruction strategies for a specific experimental paradigm, aiming for best for statistical analysis. SNAKE-fMRI answers those needs.

The SNAKE-fMRI package comes also with a complete but extensible reconstruction and statistical analysis pipeline. It provides the user with tools to reach new frontiers in data acquisition and image reconstruction strategies for fMRI and assess from an image quality and statistical analysis viewpoint multiple competing scenarios that cannot easily be ranked in advance.

Declaration of Competing Interest

The authors declare no competing financial interest.

Author Contributions

Conceptualization, Software, Visualization, Writing - Original Draft: P.-A. C.
Writing - Review & Editing: P.-A.C., P.C and A.V
Supervision, Funding Acquisition: P.C and A.V.

Software ecosystem acknowledgment

The *SNAKE-fMRI* package would not have been possible without the following existing software:

The command-line and configurations files use `hydra` (Yadan, 2019). Numerical computation involves `numpy` (Harris et al., 2020) and `scipy` (Virtanen et al., 2020). Neuroscience-related processing is performed using `nilearn` (Abraham et al., 2014) and statistical analysis is done with `scikit-learn` (Pedregosa et al., 2011).

SNAKE-fMRI was developed concurrently with other software as dependencies. MRI-related work uses `brainweb-dl` for accessing the Brain-Web dataset (Aubert-Broche et al., 2006), and `mri-nufft` for the generation and acquisition of non-Cartesian trajectories. The lazy generation of array was inspired by The reconstruction algorithms are implemented in `pysap-fmri`. The tracking and management of experiments motivated the development of `hydra-callbacks`.

Data and code availability

The *SNAKE-fMRI* Package is available at <https://github.com/paquiteau/snake-fmri>.

References

- Abraham, A., Pedregosa, F., Eickenberg, M., Gervais, P., Mueller, A., Kossaifi, J., Gramfort, A., Thirion, B., & Varoquaux, G. (2014). Machine learning for neuroimaging with scikit-learn. *Frontiers in Neuroinformatics*, 8. <https://doi.org/10.3389/fninf.2014.00014>
- Amor, Z., Comby, P.-A., Ster, C. L., Vignaud, A., & Ciuciu, P. (2023). Non-Cartesian Non-Fourier fMRI Imaging for High-Resolution Retinotopic Mapping at 7 Tesla. *2023 IEEE 9th International Workshop on Computational Advances in Multi-Sensor Adaptive Processing (CAMSAP)*, 201–205. <https://doi.org/10.1109/CAMSAP58249.2023.10403497>
- Amor, Z., Le Ster, C., Gr, C., Daval-Fr erot, G., Boulant, N., Mauconduit, F., Thirion, B., Ciuciu, P., & Vignaud, A. (2024). Impact of B_0 field imperfections correction on BOLD sensitivity in 3D-SPARKLING fMRI data. *Magnetic Resonance in Medicine*, 91(4), 1434–1448. <https://doi.org/10.1002/mrm.29943>
- Amor, Z., Radhakrishna, C. G., Ster, C. L., Daval-Fr erot, G., Boulant, N., Mauconduit, F., Mirkes, C., Ciuciu, P., & Vignaud, A. (2022). B_0 field distortions monitoring and correction for 3D non-Cartesian fMRI acquisitions using a field camera: Application to 3D-SPARKLING at 7T.
- Aubert-Broche, B., Griffin, M., Pike, G., Evans, A., & Collins, D. (2006). Twenty New Digital Brain Phantoms for Creation of Validation Image Data Bases. *IEEE Transactions on Medical Imaging*, 25(11), 1410–1416. <https://doi.org/10.1109/TMI.2006.883453>
- Beck, A., & Teboulle, M. (2009). A Fast Iterative Shrinkage-Thresholding Algorithm for Linear Inverse Problems. *SIAM Journal on Imaging Sciences*, 2(1), 183–202. <https://doi.org/10/b6wskk>
- Bennett, C. M., & Miller, M. B. (2010). How reliable are the results from functional magnetic resonance imaging? *Annals of the New York Academy of Sciences*, 1191, 133–155. <https://doi.org/10.1111/j.1749-6632.2010.05446.x>
- Bollmann, S., Kasper, L., Vannesjo, S. J., Diaconescu, A. O., Dietrich, B. E., Gross, S., Stephan, K. E., & Pruessmann, K. P. (2017). Analysis and correction of field fluctuations in fMRI data using field monitoring. *NeuroImage*, 154, 92–105. <https://doi.org/10.1016/j.neuroimage.2017.01.014>
- Brosch, J., Talavage, T., Ulmer, J., & Nyenhuis, J. (2002). Simulation of human respiration in fMRI with a mechanical model. *IEEE Transactions on Biomedical Engineering*, 49(7), 700–707. <https://doi.org/10.1109/TBME.2002.1010854>
- Button, K. S., Ioannidis, J. P. A., Mokrysz, C., Nosek, B. A., Flint, J., Robinson, E. S. J., & Munaf , M. R. (2013). Power failure: Why small sample size undermines the reliability of neuroscience. *Nature Reviews Neuroscience*, 14(5), 365–376. <https://doi.org/10.1038/nrn3475>
- Bycroft, C., Freeman, C., Petkova, D., Band, G., Elliott, L. T., Sharp, K., Motyer, A., Vukcevic, D., Delaneau, O., O’Connell, J., Cortes, A., Welsh, S., Young, A., Effingham, M., McVean, G., Leslie, S., Allen, N., Donnelly, P., & Marchini, J. (2018). The UK Biobank resource with deep phenotyping and genomic data. *Nature*, 562(7726), 203–209. <https://doi.org/10.1038/s41586-018-0579-z>
- Caballero-Gaudes, C., & Reynolds, R. C. (2017). Methods for cleaning the BOLD fMRI signal.

- NeuroImage*, 154, 128–149. <https://doi.org/10.1016/j.neuroimage.2016.12.018>
- Cakan, C., Jajcay, N., & Obermayer, K. (2023). Neurolib: A Simulation Framework for Whole-Brain Neural Mass Modeling. *Cognitive Computation*, 15(4), 1132–1152. <https://doi.org/10.1007/s12559-021-09931-9>
- Casey, B. J., Cannonier, T., Conley, M. I., Cohen, A. O., Barch, D. M., Heitzeg, M. M., Soules, M. E., Teslovich, T., Dellarco, D. V., Garavan, H., Orr, C. A., Wager, T. D., Banich, M. T., Speer, N. K., Sutherland, M. T., Riedel, M. C., Dick, A. S., Bjork, J. M., Thomas, K. M., ... Dale, A. M. (2018). The Adolescent Brain Cognitive Development (ABCD) study: Imaging acquisition across 21 sites. *Developmental Cognitive Neuroscience*, 32, 43–54. <https://doi.org/10.1016/j.dcn.2018.03.001>
- Chaithya, G. R., Weiss, P., Daval-Fr erot, G., Massire, A., Vignaud, A., & Ciuciu, P. (2022). Optimizing Full 3D SPARKLING Trajectories for High-Resolution Magnetic Resonance Imaging. *IEEE Transactions on Medical Imaging*, 41(8), 2105–2117. <https://doi.org/10.1109/TMI.2022.3157269>
- Chen, X., Lu, B., & Yan, C.-G. (2018). Reproducibility of R-fMRI metrics on the impact of different strategies for multiple comparison correction and sample sizes. *Human Brain Mapping*, 39(1), 300–318. <https://doi.org/10.1002/hbm.23843>
- Chen, Z., Robinson, J., & Calhoun, V. (2018). Brain functional BOLD perturbation modelling for forward fMRI and inverse mapping. *PLoS ONE*, 13(1), e0191266. <https://doi.org/10.1371/journal.pone.0191266>
- Cheng, H., Zhao, Q., Duensing, G. R., Edelstein, W. A., Spencer, D., Browne, N., Saylor, C., & Limkeman, M. (2006). SmartPhantom — an fMRI simulator. *Magnetic Resonance Imaging*, 24(3), 301–313. <https://doi.org/10.1016/j.mri.2005.12.012>
- Chiew, M., Graedel, N. N., & Miller, K. L. (2018). Recovering task fMRI signals from highly under-sampled data with low-rank and temporal subspace constraints. *NeuroImage*, 174, 97–110. <https://doi.org/10.1016/j.neuroimage.2018.02.062>
- Ciuciu, P., Poline, J.-B., Marrelec, G., Idier, J., Pallier, C., & Benali, H. (2003). Unsupervised robust non-parametric estimation of the hemodynamic response function for any fMRI experiment. 22(10), 1235–1251.
- Comby, P.-A., Daval-Fr erot, G., Gr, C., Vignaud, A., & Ciuciu, P. (2024). MRI-NUFFT: An open source Python package to make non-Cartesian MR Imaging easier. *ISMRM Annual Meeting*, (in Press).
- Donoho, D., & Johnstone, I. (1994). Threshold selection for wavelet shrinkage of noisy data. *Proceedings of 16th Annual International Conference of the IEEE Engineering in Medicine and Biology Society*, A24–A25. <https://doi.org/10.1109/IEMBS.1994.412133>
- Drobnjak, I., Gavaghan, D., S uli, E., Pitt-Francis, J., & Jenkinson, M. (2006). Development of a functional magnetic resonance imaging simulator for modeling realistic rigid-body motion artifacts. *Magnetic Resonance in Medicine*, 56(2), 364–380. <https://doi.org/10.1002/mrm.20939>
- Duerst, Y., Wilm, B. J., Dietrich, B. E., Vannesjo, S. J., Barmet, C., Schmid, T., Brunner, D. O., & Pruessmann, K. P. (2015). Real-time feedback for spatiotemporal field stabilization in MR systems. *Magnetic Resonance in Medicine*, 73(2), 884–893. <https://doi.org/10.1002/mrm.25167>
- El Gueddari, L., Ciuciu, P., Chouzenoux, E., Vignaud, A., & Pesquet, J.-C. (2019). Calibrationless oscar-based image reconstruction in compressed sensing parallel MRI. *2019 IEEE 16th International Symposium on Biomedical Imaging (ISBI 2019)*, 1532–1536. <https://doi.org/10/ghw8zr>
- El Gueddari, L., Giliyar Radhakrishna, C., Chouzenoux, E., & Ciuciu, P. (2021). Calibration-less multi-coil compressed sensing magnetic resonance image reconstruction based on OSCAR regularization. *Journal of Imaging*, 7(3), 58.
- Elam, J. S., Glasser, M. F., Harms, M. P., Sotiropoulos, S. N., Andersson, J. L. R., Burgess, G. C., Curtiss, S. W., Oostenveld, R., Larson-Prior, L. J., Schoffelen, J.-M., Hodge, M. R., Cler, E. A., Marcus, D. M., Barch, D. M., Yacoub, E., Smith, S. M., Ugur-

- bil, K., & Van Essen, D. C. (2021). The Human Connectome Project: A retrospective. *NeuroImage*, 244, 118543. <https://doi.org/10.1016/j.neuroimage.2021.118543>
- Ellis, C. T., Baldassano, C., Schapiro, A. C., Cai, M. B., & Cohen, J. D. (2020). Facilitating open-science with realistic fMRI simulation: Validation and application. *PeerJ*, 8, e8564. <https://doi.org/10.7717/peerj.8564>
- Erhardt, E. B., Allen, E. A., Wei, Y., Eichele, T., & Calhoun, V. D. (2012). SimTB, a simulation toolbox for fMRI data under a model of spatiotemporal separability. *NeuroImage*, 59(4), 4160–4167. <https://doi.org/10.1016/j.neuroimage.2011.11.088>
- Esteban, O., Markiewicz, C. J., Blair, R. W., Moodie, C. A., Isik, A. I., Erramuzpe, A., Kent, J. D., Goncalves, M., DuPre, E., Snyder, M., Oya, H., Ghosh, S. S., Wright, J., Durnez, J., Poldrack, R. A., & Gorgolewski, K. J. (2019). fMRIPrep: A robust preprocessing pipeline for functional MRI. *Nature Methods*, 16(1), 111–116. <https://doi.org/10.1038/s41592-018-0235-4>
- Farrens, S., Grigis, A., El Gueddari, L., Ramzi, Z., Chaithya, G. R., Starck, S., Sarthou, B., Cherkaoui, H., Ciuciu, P., & Starck, J.-L. (2020). PySAP: Python sparse data analysis package for multidisciplinary image processing. *Astronomy and Computing*, 32, 100402. <https://doi.org/10/ghw8zm>
- Fessler, J. A. (2019, June 13). *Optimization methods for MR image reconstruction (long version)*. arXiv: 1903.03510 [eess, math].
- Gach, H. M., Tanase, C., & Boada, F. (2008). 2D & 3D Shepp-Logan Phantom Standards for MRI. *2008 19th International Conference on Systems Engineering*, 521–526. <https://doi.org/10.1109/ICSEng.2008.15>
- The General Linear Model. (2019, September 17). In *Statistical Analysis of fMRI Data, second edition*. MIT Press.
- Glover, G. H. (1999). Deconvolution of Impulse Response in Event-Related BOLD fMRI1. *NeuroImage*, 9(4), 416–429. <https://doi.org/10.1006/nimg.1998.0419>
- Gorgolewski, K., Burns, C., Madison, C., Clark, D., Halchenko, Y., Waskom, M., & Ghosh, S. (2011). Nipype: A Flexible, Lightweight and Extensible Neuroimaging Data Processing Framework in Python. *Frontiers in Neuroinformatics*, 5. <https://doi.org/10.3389/fninf.2011.00013>
- Gorgolewski, K. J., Auer, T., Calhoun, V. D., Craddock, R. C., Das, S., Duff, E. P., Flandin, G., Ghosh, S. S., Glatard, T., Halchenko, Y. O., Handwerker, D. A., Hanke, M., Keator, D., Li, X., Michael, Z., Maumet, C., Nichols, B. N., Nichols, T. E., Pellman, J., . . . Poldrack, R. A. (2016). The brain imaging data structure, a format for organizing and describing outputs of neuroimaging experiments. *Scientific Data*, 3(1), 160044. <https://doi.org/10.1038/sdata.2016.44>
- Graedel, N. N., Miller, K. L., & Chiew, M. (2022). Ultrahigh Resolution fMRI at 7T Using Radial-Cartesian TURBINE Sampling. *Magnetic Resonance in Medicine*, 88(5), 2058–2073. <https://doi.org/10.1002/mrm.29359>
- Guerquin-Kern, M., Lejeune, L., Pruessmann, K. P., & Unser, M. (2012). Realistic Analytical Phantoms for Parallel Magnetic Resonance Imaging. *IEEE Transactions on Medical Imaging*, 31(3), 626–636. <https://doi.org/10.1109/TMI.2011.2174158>
- Harris, C. R., Millman, K. J., van der Walt, S. J., Gommers, R., Virtanen, P., Cournapeau, D., Wieser, E., Taylor, J., Berg, S., Smith, N. J., Kern, R., Picus, M., Hoyer, S., van Kerkwijk, M. H., Brett, M., Haldane, A., Del Río, J. F., Wiebe, M., Peterson, P., . . . Oliphant, T. E. (2020). Array programming with NumPy. *Nature*, 585(7825), 357–362. <https://doi.org/10.1038/s41586-020-2649-2>
- Huang, H., Yang, Q., Wang, J., Zhang, P., Cai, S., & Cai, C. (2023). High-efficient Bloch simulation of magnetic resonance imaging sequences based on deep learning [Comment: 18 pages, 8 figures]. *Physics in Medicine & Biology*, 68(8), 085002. <https://doi.org/10.1088/1361-6560/acc4a6>
- Inati, S. J., Naegele, J. D., Zwart, N. R., Roopchansingh, V., Lizak, M. J., Hansen, D. C., Liu, C.-Y., Atkinson, D., Kellman, P., Kozerke, S., Xue, H., Campbell-Washburn, A. E., Sørensen, T. S., & Hansen, M. S. (2017). ISMRM Raw data format: A proposed standard for MRI raw datasets. *Magnetic Resonance in Medicine*, 77(1), 411–421. <https://doi.org/10.1002/mrm.26089>

- Jamil, R., Mauconduit, F., Le Ster, C., Ehses, P., Poser, B. A., Vignaud, A., & Boulant, N. (2021). Temporal SNR optimization through RF coil combination in fMRI: The more, the better? *PLoS ONE*, *16*(11), e0259592. <https://doi.org/10.1371/journal.pone.0259592>
- Jochimsen, T. H., Schäfer, A., Bammer, R., & Moseley, M. E. (2006). Efficient simulation of magnetic resonance imaging with Bloch–Torrey equations using intra-voxel magnetization gradients. *Journal of Magnetic Resonance*, *180*(1), 29–38. <https://doi.org/10.1016/j.jmr.2006.01.001>
- Kim, D., & Fessler, J. A. (2018). Adaptive Restart of the Optimized Gradient Method for Convex Optimization. *Journal of Optimization Theory and Applications*, *178*(1), 240–263. <https://doi.org/10/gdvch7>
- Kose, R., & Kose, K. (2017). BlochSolver: A GPU-optimized fast 3D MRI simulator for experimentally compatible pulse sequences. *Journal of Magnetic Resonance*, *281*, 51–65. <https://doi.org/10.1016/j.jmr.2017.05.007>
- Kumar, R., Tan, L., Kriegstein, A., Lithen, A., Polimeni, J. R., Mujica-Parodi, L. R., & Strey, H. H. (2021). Ground-truth “resting-state” signal provides data-driven estimation and correction for scanner distortion of fMRI time-series dynamics. *NeuroImage*, *227*, 117584. <https://doi.org/10.1016/j.neuroimage.2020.117584>
- Le Ster, C., Grant, A., Van de Moortele, P.-F., Monreal-Madrigal, A., Adriany, G., Vignaud, A., Mauconduit, F., Rabrait-Lerman, C., Poser, B. A., Uğurbil, K., & Boulant, N. (2022). Magnetic field strength dependent SNR gain at the center of a spherical phantom and up to 11.7T. *Magnetic Resonance in Medicine*, *88*(5), 2131–2138. <https://doi.org/10.1002/mrm.29391>
- Lewis, L. D., Setsompop, K., Rosen, B. R., & Polimeni, J. R. (2016). Fast fMRI can detect oscillatory neural activity in humans. *Proceedings of the national academy of sciences*, *113*(43), E6679–E6685.
- Lewis, L. D., Setsompop, K., Rosen, B. R., & Polimeni, J. R. (2018). Stimulus-dependent hemodynamic response timing across the human subcortical-cortical visual pathway identified through high spatiotemporal resolution 7T fMRI. *Neuroimage*, *181*, 279–291.
- Lin, C. Y., & Fessler, J. A. (2019). Efficient Dynamic Parallel MRI Reconstruction for the Low-Rank Plus Sparse Model. *IEEE Transactions on Computational Imaging*, *5*(1), 17–26. <https://doi.org/10.1109/TCI.2018.2882089>
- Liu, F., Velikina, J. V., Block, W. F., Kijowski, R., & Samsonov, A. A. (2017). Fast Realistic MRI Simulations Based on Generalized Multi-Pool Exchange Tissue Model. *IEEE Transactions on Medical Imaging*, *36*(2), 527–537. <https://doi.org/10.1109/TMI.2016.2620961>
- Marek, S., Tervo-Clemmens, B., Calabro, F. J., Montez, D. F., Kay, B. P., Hatoum, A. S., Donohue, M. R., Foran, W., Miller, R. L., Hendrickson, T. J., Malone, S. M., Kandala, S., Feczko, E., Miranda-Dominguez, O., Graham, A. M., Earl, E. A., Perrone, A. J., Cordova, M., Doyle, O., . . . Dosenbach, N. U. F. (2022). Reproducible brain-wide association studies require thousands of individuals. *Nature*, *603*(7902), 654–660. <https://doi.org/10.1038/s41586-022-04492-9>
- Muresan, L., Renken, R., Roerdink, J., & Duifhuis, H. (2005). Automated Correction of Spin-History Related Motion Artefacts in fMRI: Simulated and Phantom Data. *IEEE Transactions on Biomedical Engineering*, *52*(8), 1450–1460. <https://doi.org/10.1109/TBME.2005.851484>
- Nakuci, J., Wasylshyn, N., Cieslak, M., Elliott, J. C., Bansal, K., Giesbrecht, B., Grafton, S. T., Vettel, J. M., Garcia, J. O., & Muldoon, S. F. (2023). Within-subject reproducibility varies in multi-modal, longitudinal brain networks. *Scientific Reports*, *13*(1), 6699. <https://doi.org/10.1038/s41598-023-33441-3>
- Ogawa, S., Lee, T.-M., Kay, A. R., & Tank, D. W. (1990). Brain magnetic resonance imaging with contrast dependent on blood oxygenation. *proceedings of the National Academy of Sciences*, *87*(24), 9868–9872.
- Ong Frank & Lustig Michael. (2019). SigPy: A Python Package for High Performance Iterative Reconstruction. *ISMRM 2019*.

- Otazo, R., Candès, E., & Sodickson, D. K. (2015). Low-rank plus sparse matrix decomposition for accelerated dynamic MRI with separation of background and dynamic components. *Magnetic Resonance in Medicine*, 73(3), 1125–1136. <https://doi.org/10/f8c3ct>
- Pedregosa, F., Varoquaux, G., Gramfort, A., Michel, V., Thirion, B., Grisel, O., Blondel, M., Prettenhofer, P., Weiss, R., Dubourg, V., Vanderplas, J., Passos, A., Cournapeau, D., Brucher, M., Perrot, M., & Duchesnay, E. (2011). Scikit-learn: Machine learning in Python. *Journal of Machine Learning Research*, 12, 2825–2830.
- Peretti, L., Donatelli, G., Cencini, M., Cecchi, P., Buonincontri, G., Cosottini, M., Tosetti, M., & Costagli, M. (2023). Generating Synthetic Radiological Images with PySynthMRI: An Open-Source Cross-Platform Tool. *Tomography*, 9(5), 1723–1733. <https://doi.org/10.3390/tomography9050137>
- Petersson, J. S., Christoffersson, J. .-, & Golman, K. (1993). MRI simulation using the k-space formalism. *Magnetic Resonance Imaging*, 11(4), 557–568. [https://doi.org/10.1016/0730-725X\(93\)90475-S](https://doi.org/10.1016/0730-725X(93)90475-S)
- Petrov, A. Y., Herbst, M., & Andrew Stenger, V. (2017). Improving temporal resolution in fMRI using a 3D spiral acquisition and low rank plus sparse (L+S) reconstruction. *NeuroImage*, 157, 660–674. <https://doi.org/10/gbwwvz>
- Pinaya, W. H. L., Graham, M. S., Kerfoot, E., Tudosiu, P.-D., Dafflon, J., Fernandez, V., Sanchez, P., Wolleb, J., da Costa, P. F., Patel, A., Chung, H., Zhao, C., Peng, W., Liu, Z., Mei, X., Lucena, O., Ye, J. C., Tsaftaris, S. A., Dogra, P., . . . Cardoso, M. J. (2023, July 27). *Generative AI for Medical Imaging: Extending the MONAI Framework*. arXiv: 2307.15208 [cs, eess].
- Pipe, J. G., & Menon, P. (1999). Sampling density compensation in MRI: Rationale and an iterative numerical solution. *Magnetic Resonance in Medicine*, 41(1), 179–186. [https://doi.org/10.1002/\(SICI\)1522-2594\(199901\)41:1<179::AID-MRM25>3.0.CO;2-V](https://doi.org/10.1002/(SICI)1522-2594(199901)41:1<179::AID-MRM25>3.0.CO;2-V)
- Polimeni, J. R., & Lewis, L. D. (2021). Imaging faster neural dynamics with fast fMRI: a need for updated models of the hemodynamic response. *Progress in neurobiology*, 207, 102174.
- Sanz Leon, P., Knock, S., Woodman, M., Domide, L., Mersmann, J., McIntosh, A., & Jirsa, V. (2013). The Virtual Brain: A simulator of primate brain network dynamics. *Frontiers in Neuroinformatics*, 7. <https://doi.org/10.3389/fninf.2013.00010>
- Schirner, M., Domide, L., Perdakis, D., Triebkorn, P., Stefanovski, L., Pai, R., Prodan, P., Valean, B., Palmer, J., Langford, C., Blickensdörfer, A., van der Vlag, M., Diaz-Pier, S., Peyser, A., Klijn, W., Pleiter, D., Nahm, A., Schmid, O., Woodman, M., . . . Ritter, P. (2022). Brain simulation as a cloud service: The Virtual Brain on EBRAINS. *NeuroImage*, 251, 118973. <https://doi.org/10.1016/j.neuroimage.2022.118973>
- Stöcker, T., Vahedipour, K., Pflugfelder, D., & Shah, N. J. (2010). High-performance computing MRI simulations. *Magnetic Resonance in Medicine*, 64(1), 186–193. <https://doi.org/10.1002/mrm.22406>
- Sutton, B., Noll, D., & Fessler, J. (2003). Fast, iterative image reconstruction for MRI in the presence of field inhomogeneities. *IEEE Transactions on Medical Imaging*, 22(2), 178–188. <https://doi.org/10.1109/TMI.2002.808360>
- Szucs, D., & Ioannidis, J. P. A. (2017). Empirical assessment of published effect sizes and power in the recent cognitive neuroscience and psychology literature. *PLOS Biology*, 15(3), e2000797. <https://doi.org/10.1371/journal.pbio.2000797>
- Triantafyllou, C., Polimeni, J. R., & Wald, L. L. (2011). Physiological noise and signal-to-noise ratio in fMRI with multi-channel array coils. *NeuroImage*, 55(2), 597–606. <https://doi.org/10.1016/j.neuroimage.2010.11.084>
- Uecker, M., Ong, F., & Tamir, J. (2015). Berkeley advanced reconstruction toolbox. *Proc. Intl. Soc. Mag. Reson. Med.* 23.
- van der Zwaag, W., Marques, J. P., Kober, T., Glover, G., Gruetter, R., & Krueger, G. (2012). Temporal SNR characteristics in segmented 3D-EPI at 7T. *Magnetic Resonance in Medicine*, 67(2), 344–352. <https://doi.org/10.1002/mrm.23007>

- Viessmann, O., & Polimeni, J. R. (2021). High-resolution fMRI at 7 Tesla: Challenges, promises and recent developments for individual-focused fMRI studies. *Current opinion in behavioral sciences*, *40*, 96–104. <https://doi.org/10.1016/j.cobeha.2021.01.011>
- Vincent, T., Badillo, S., Risser, L., Chaari, L., Bakhou, C., Forbes, F., & Ciuciu, P. (2014). Flexible multivariate hemodynamics fMRI data analyses and simulations with PyHRF. *Frontiers in Neuroscience*, *8*. <https://doi.org/10.3389/fnins.2014.00067>
- Virtanen, P., Gommers, R., Oliphant, T. E., Haberland, M., Reddy, T., Cournapeau, D., Burovski, E., Peterson, P., Weckesser, W., Bright, J., van der Walt, S. J., Brett, M., Wilson, J., Millman, K. J., Mayorov, N., Nelson, A. R. J., Jones, E., Kern, R., Larson, E., . . . van Mulbregt, P. (2020). SciPy 1.0: Fundamental algorithms for scientific computing in Python. *Nature Methods*, *17*(3), 261–272. <https://doi.org/10.1038/s41592-019-0686-2>
- Welvaert, M., Durnez, J., Moerkerke, B., Berdoolaege, G., & Rosseel, Y. (2011). neuRosim: An R Package for Generating fMRI Data. *Journal of Statistical Software*, *44*, 1–18. <https://doi.org/10.18637/jss.v044.i10>
- Welvaert, M., & Rosseel, Y. (2014). A Review of fMRI Simulation Studies. *PLOS ONE*, *9*(7), e101953. <https://doi.org/10.1371/journal.pone.0101953>
- Xanthis, C. G., Venetis, I. E., Chalkias, A. V., & Aletras, A. H. (2014). MRISIMUL: A GPU-Based Parallel Approach to MRI Simulations. *IEEE Transactions on Medical Imaging*, *33*(3), 607–617. <https://doi.org/10.1109/TMI.2013.2292119>
- Yadan, O. (2019). Hydra - A framework for elegantly configuring complex applications.
- Ye, J. C., Tak, S., Han, Y., & Park, H. W. (2007). Projection reconstruction MR imaging using FOCUSS. *Magnetic Resonance in Medicine*, *57*(4), 764–775.

SNAKE-fMRI: A modular fMRI data simulator
from the space-time domain to k-space and back.
Supplementary material.

A Interacting with SNAKE-fMRI

A.1 Create your custom handler

Due to the modularity of Snake-fMRI it is easy to add your own modeling steps. Here we propose a simple example that adds scanner drift to the acquired data.

```
import numpy as np
from nilearn.glm.first_level.design_matrix import _make_drift
from snkf.handlers import AbstractHandler, requires_field

@requires_field("data_acq") # ensure that simulation has the required data.
class PolynomialScannerDriftHandler(AbstractHandler):
    """Add Polynomial drift to the data."""

    __handler_name__ = "scanner-polydrift"

    # parameters for the Handler, dataclass-like definition.
    drift_order: int
    drift_intensities: np.ndarray

    def _handle(self, sim):
        # Nilearn does the heavy lifting
        frames_tr = np.linspace(0, sim.sim_time, sim.n_frames)
        drift_matrix = _make_drift("polynomial", frame_times=frames_tr, order=self.drift_order)
        drift_matrix = drift_matrix[:, :-1] # remove intercept column
        drift_intensity = np.linspace(1, 1 + self.drift_intensities, sim.n_frames)
        timeseries = drift_intensity @ drift_matrix
        sim.data_acq[:, sim.static_vol > 0] *= timeseries[:, np.newaxis] # apply drift
        return sim
```

A.2 Declaring a new simulation

Now we can create a new simulation using our handler. More examples of handlers usage are available in *SNAKE-fMRI* documentation.

```
from snkf.simulation import SimData
from my_local_package import ScannerDriftHandler
from snkf.handlers import H

sim = SimData(shape=(64,64), fov=(.192, .192), sim_time=300, sim_tr= 0.1, )
simulator = H["phantom-big"] >> H["activation-block"] >> H["scanner-poly-drift"]
sim = simulator(sim) # update the simulation by running it through the handlers.
```

A simulation can also be described using a configuration file, using [hydra](#) conventions:

```

defaults:
- handlers:
  - phantom-brainweb
  - activation-block
  - noise-gaussian
  - acquisition-vds
- reconstructors: adjoint
- _self_

cache_dir: ${oc.env:PWD}/cache

sim_params:
  sim_tr: 0.1      # time resolution in image domain (s)
  sim_time: 300    # total time of experiments
  shape: [-1,-1,-1] # inherited from phantom
  fov: [-1,-1,-1] # inherited from phantom.
  n_coils: 1      # single coil for fast computations
  rng: 19980408   # random seed
  lazy: True      # Use the lazy generation of volume.

handlers:
  phantom-brainweb: # Create the phantom
    sub_id: 5
    bbox: [0.225,-0.07, 0.06, -0.055, null, null] # reduce the FOV to exclude spine
    brainweb_folder: ${cache_dir}/brainweb
    res: [3.0, 3.0, 3.0] # resolution in mm
  activation-block: # Add bold signal
    event_name: block_on
    block_on: 20
    block_off: 20
    duration: 300
    bold_strength: 0.02
  noise-gaussian: # add gaussian noise
    snr: 10
  acquisition-vds: # perform acquisition, fully sampled is a special case of VDS sampling.
    shot_time_ms: 50
    acs: 1
    accel: 1
    accel_axis: -1
    constant: true
    order: TOP_DOWN
    smaps: false

reconstructors:
  adjoint: {} # Simple FFT reconstruction.

stats:
  contrast_name: ${handlers.activation-block.event_name}

```

All configuration files for running the scenarios described in the manuscript are available in the snake-fmri repository. After installation they can be run as follows:

```

$ pip install snake-fmri
$ snkf-main --config-name="scenario1"
# Using Hydra, parameters can be modified and run over a grid of parameter.
$ snkf-main --config-name="scenario2" -m ++reconstructors.sequential.restart_strategy=cold,warm,refine

```

B Study of SNR impact in Scenario 1

To help analyse the impact of input SNR (SNR_i) on the results we performed simulation with a sweep of different SNR values as well as the number of coils in the setup of Scenario S1. The reconstruction being a simple linear operation (Smaps combination and Inverse fourier transform) we can directly see the impact on the reconstruction.

The addition of uniform gaussian noise in the image results in the degradation of image quality metrics, in a linear fashion (Figure 1). For $tSNR$, the relation follows the same principle. Overall, setting $SNR_i = 10$ as in our scenarios, provides a realistic $SNR_{exp} \simeq 40$ and $tSNR \simeq 30$. This reproduces a thermal noise dominant setting, which particularly occurs at high resolution.

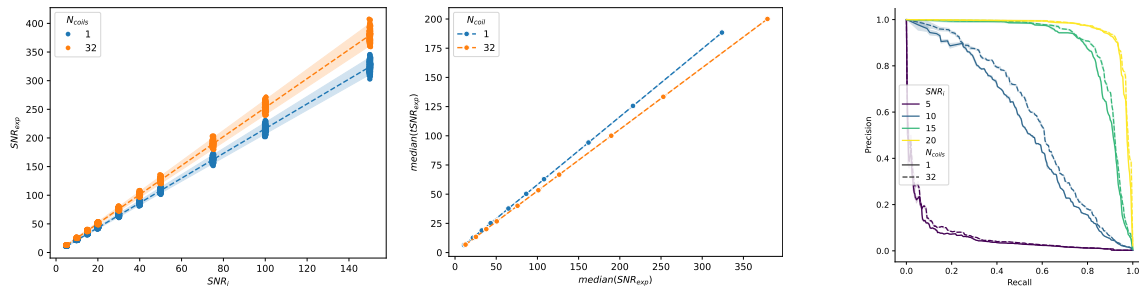


Figure 1: Impact of input SNR in Scenario 1 on image quality and statistics.

C Non-Cartesian trajectories design and expansion

By combining SNAKE-fMRI with MRI-NUFFT, it is possible to create and explore non-Cartesian trajectories, and small example of base trajectories (2D shots) and expansions (stack, rotate, conify) are represented on Figure 2.

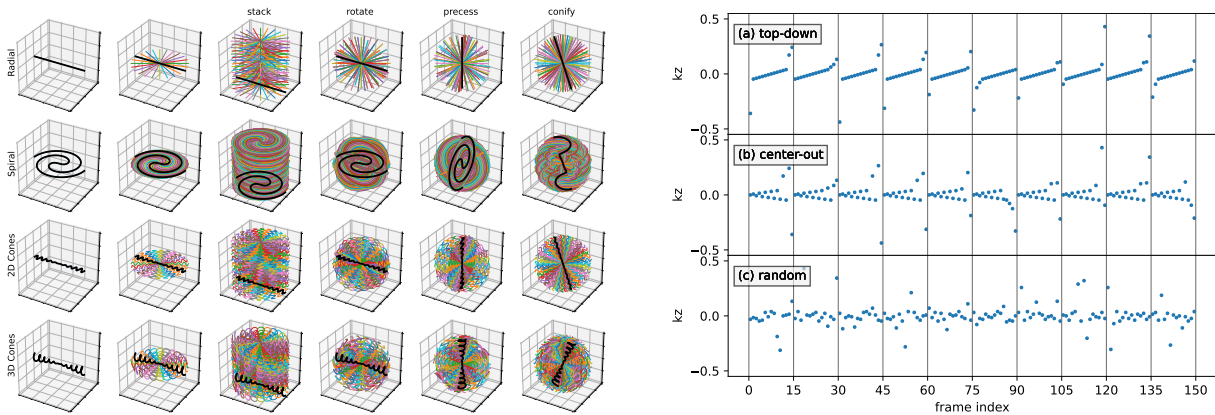


Figure 2: Left: Overview of trajectories generation possible with MRI-NUFFT. Right: Further expansions available in *SNAKE-fMRI* over the time axis are also possible, notably in which order the shot of each k-space frames are acquired, here for a stacked acquisition